NUMERICAL ANALYSIS OF HEAT AND MASS TRANSFER IN HEAT PIPE USING A TRIPLE-PHASE COUPLED MODEL

ZanXiu WU, HuanXin LAI*

School of Mechanical and Power Engineering, East China University of Science and Technology, Shanghai, China

*Corresponding author email: hlai@ecust.edu.cn

A numerical prediction model is proposed to analyze the performance of heat pipe. The model is transient and applicable to both cylindrical and Cartesian coordinate systems. The vapor flow within the vapor core, the non-Darcian liquid flow within the porous wick, and the phase change processes at the vapor-liquid interface are considered. The triple-phase coupling is realized through boundary conditions, imposed using user-defined functions (UDFs). The model is employed to solve the hydraulic and heat transfer performance of heat pipes. A flat heat pipe and a cylindrical heat pipe are calculated to validate the model. Both steady and transient characteristics of the flat heat pipe are studied. It is found that the variation tendencies of the wall temperature difference, velocity and pressure drop of vapor and liquid are consistent. As heating power changes from 10 to 50 W, the maximum wall temperature difference rises from 0.75 to 2.41 K. The maximum velocity of vapor and liquid increases by 2.977 m/s and 9.72×10^{-5} m/s, respectively. Additionally, the maximum pressure drop of vapor and liquid increases by 13.9 and 42 Pa, respectively. The heating power is found to be critical for the flow characteristics.

Key words: heat pipe; triple-phase coupled model; transient model; numerical simulation; heating power

1. Introduction

In recent years, with the development of portable electronic products towards compactness, integration, and high performance. These demands have imposed serious challenges for efficient thermal management of high-power and miniaturized electronic devices [1]. Due to excellent thermal management capabilities, heat pipes are widely used in cutting-edge fields such as aerospace, electronic communications, new energy vehicles, high-performance computing, and precision instruments [2]. The heat pipe is a closed element, its internal flow field is hard to measure experimentally. Therefore, the computational fluid dynamics (CFD) methods become important in studying the fluid flow and heat transfer inside the heat pipe. However, due to the transfer of heat, mass, and momentum inside the heat pipe, as well as the complex physical processes of evaporation and condensation, there are many difficulties in analyzing the flow and heat transfer characteristics of heat pipe by conventional numerical methods [3]. In particular, the strong coupling between the temperature, pressure, and velocity fields at the interface caused by phase change, increases the complexity and difficulty.

Some progress has been made in the development of numerical and analytical models for the heat pipe in the past decades [4]. The models for numerical simulations of heat pipes reported in the literature can be classified into steady and transient models. In the steady models, Annamalai et al. [5] developed a three-dimensional steady model, the ideal gas equation is used to calculate the vapor temperature under constant pressure. Pooyoo et al. [6] employed a three-dimensional steady model with non-Darcian transport in porous media, simulating evaporation and condensation via mass inlet and outlet boundaries to determine vapor and liquid velocity distributions in the heat pipe. In transient models, Chen et al. [7] developed a two-dimensional transient prediction model to study the effect of channel geometry variations on the heat pipe performance. Li et al. [8] used a three-dimensional transient model to study non-isothermal flow and phase change, investigating the impact of wire mesh wick on hydraulic and thermal performance in ultra-thin vapor chambers. The above research results are highly significant for the numerical modeling of heat pipes. However, due to dynamic variations at the vapor-liquid interface and the phase change under transient conditions, the fluid dynamics and heat transfer in heat pipes are highly complex. The strong coupling between vapor, liquid, and solid phases remains poorly understood, while significant challenges remain in accurately predicting the overall performance of heat pipes.

Meanwhile, the above-mentioned numerical prediction models reported in the literature are only applicable to physical models in a single coordinate system (Cartesian coordinate system or cylindrical coordinate system), which limits their general applicability. In order to extend the application scope of the prediction model, the Cartesian and cylindrical coordinate systems are unified in this paper, and a two-dimensional transient numerical prediction model for triple-phase coupling is established. So both the cylindrical and flat plate heat pipes can be considered. The porous media model and user-defined functions (UDFs) are used to simulate the fluid flow and heat transfer inside the heat pipes. The transient characteristics during the start-up phase and the steady-state characteristics under stable operation conditions are studied. The transient thermal and hydraulic response is quantified by examining the temporal evolution of temperature and flow fields, while the steady-state characteristics are assessed by evaluating key indicators, such as the overall thermal resistance and total pressure drop across a range of heating power. Furthermore, the critical physical fields, including the outside wall temperature distribution, the internal pressure variation, and the fluid velocity profiles are analyzed to identify the physical mechanisms governing performance limitations. The study is intended to provide a reference for the optimization and design of the heat pipes.

2. Physical model

The cylindrical and the flat heat pipes from references [9] and [10], respectively, are considered. The computational domains are shown in Fig. 1 and Fig. 2. The material of the solid wall and the porous wick is copper. The working medium is water at 294.15 K, liquid and vapor fill the wick and the vapor core, respectively.

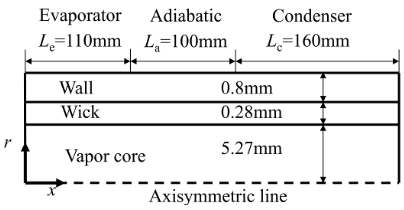

Figure 1. Computational domain of cylindrical heat pipe

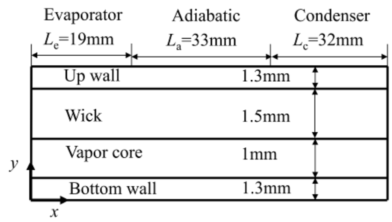

Figure 2. Computational domain of flat heat pipe

3. Numerical methods

3.1. Assumptions

For simplicity of descriptions, the following assumptions are made in this paper [8-9]:

1) Under initial conditions, the vapor core and wick are filled with saturated vapor and liquid, respectively. i.e., only single-phase flows in the two regions are considered.

2) The fluid flows in both the wick and the vapor core are assumed to be laminar, while the vapor is assumed to follow the ideal gas law.

3) Phase change is restricted to happen at the vapor-liquid interface. and the evaporation and condensation accommodation coefficients are identical.

4) The wick liquid remains below the nucleate boiling threshold.

5) Except for density, the physical properties of the vapor and liquid remain constant.

6) Gravity is neglected in the horizontally oriented heat pipes. In such configuration, the gravity is vertical to central axis of the heat pipe, it neither assists nor hinders the axial flow of liquid. Consequently, the capillary force within the wick serves as the dominant mechanism driving the circulation flow, making gravitational effects negligible.

3.2. Governing equations

Based on the above assumptions, the continuity equation for the wick and vapor core is:

$$\varepsilon\frac{\partial\rho}{\partial t}+\frac{\partial(\rho u)}{\partial x}+\frac{\partial(r\rho v)}{r\partial y}=0 \tag{1}$$

where $r=1$ represents the governing equation in the Cartesian coordinate system, $r=y$ represents the governing equation in the cylindrical coordinate system. ε is the porosity of the wick, ρ is the fluid density, u and represents the velocity components in the *x* (axial) and *y* (radial) directions, respectively.

The momentum equations for the wick and vapor core:

$$\varepsilon\frac{\partial(\rho u)}{\partial t}+\frac{\partial(r\rho uu)}{r\partial x}+\frac{\partial(r\rho vu)}{r\partial y}=-\frac{\varepsilon\partial P}{\partial x}+\mu\left[\frac{\partial}{\partial x}(\frac{\partial u}{\partial x})+\frac{1}{r}\frac{\partial}{\partial y}(r\frac{\partial u}{\partial y})\right]-\frac{\mu\varepsilon u}{K}-\frac{C_E\varepsilon\rho\left|\vec{u}\right|}{K^{\frac{1}{2}}}u \tag{2}$$

$$\varepsilon\frac{\partial(\rho v)}{\partial t}+\frac{\partial(r\rho uv)}{r\partial x}+\frac{\partial(r\rho vv)}{r\partial y}=-\frac{\varepsilon\partial P}{\partial y}+\mu\left[\frac{\partial}{\partial x}(\frac{\partial v}{\partial x})+\frac{1}{r}\frac{\partial}{\partial y}(r\frac{\partial v}{\partial y})\right]-\frac{\mu\varepsilon v}{K}-\frac{C_E\varepsilon\rho\left|\vec{u}\right|}{K^{\frac{1}{2}}}v \tag{3}$$

where P is the pressure, μ is the dynamic viscosity coefficient; K is permeability, $\vec{u}$ is the velocity vector. In the vapor core $K=\infty$ and $\varepsilon=1$, the Ergun coefficient C_E is calculated from the Ergun equation：

$$C_E=\frac{1.75}{\sqrt{150\varepsilon^2}} \tag{4}$$

The porosity and permeability of the copper screen mesh wick can be calculated as follows [8]:

$$\varepsilon=1-\frac{1.05\pi Md}{4} \tag{5}$$

$$K=\frac{d^2\varepsilon^3}{122(1-\varepsilon)^2} \tag{6}$$

where *d* and *M* are the diameter and the number of copper screen mesh, respectively.

The energy equations for the solid wall, wick, and vapor core:

$$\frac{\partial T}{\partial t}(\rho C)_n = \frac{\partial}{\partial x}(k\frac{\partial T}{\partial x}) + \frac{1}{r}\frac{\partial}{\partial y}(rk\frac{\partial T}{\partial y}) \tag{7}$$

In Eq. (7), n represents the different calculation domain, C is the specific heat capacity of different phase, k is the thermal conductivity of different phase, T is the temperature.

3.3. Boundary conditions

As shown in Fig. 1, the boundaries of the outside wall of heat pipe are as follows:

$$\begin{cases} -k_s \dfrac{\partial T}{\partial y} = q & \text{evaporator} \\ -k_s \dfrac{\partial T}{\partial y} = 0 & \text{adiabatic} \\ -k_s \dfrac{\partial T}{\partial y} = h_\infty (T - T_\infty) & \text{condenser} \end{cases} \tag{8}$$

where q is the heat flux, h_∞ is the convective heat transfer coefficient, T and T_∞ are wall and cooling fluid temperature.

The lateral walls are adiabatic with a no-slip boundary:

$$\frac{\partial T}{\partial x} = 0 \tag{9}$$

$$u = v = 0 \tag{10}$$

The boundary at the wall-wick interface is written as:

$$\frac{k_w}{\Delta r_w}\left(T_{s-w} - T_w\right) = \frac{k_s}{\Delta r_s}\left(T_s - T_{s-w}\right) \tag{11}$$

$$u = v = 0 \tag{12}$$

where k_w and k_s are the thermal conductivity of wick and solid, T_w and T_s are the temperature of the wall and wick cells adjacent to the wall-wick interface, T_{s-w} is temperature of the wall-wick interface, Δr_w and Δr_s is the distance from and wick cell centers to the interface, respectively.

For the wall domain, the temperature at the wall-wick interface is given by Eq. (13):

$$T_{s-w} = \frac{\dfrac{k_w}{\Delta r_w}T_w + \dfrac{k_s}{\Delta r_s}T_s}{\dfrac{k_w}{\Delta r_w} + \dfrac{k_s}{\Delta r_s}} \tag{13}$$

For the wick domain, the temperature at the wick-wall interface is given by Eq. (14):

$$T_{s-w} = T_{w-s} \tag{14}$$

Where T_{w-s} is temperature of the wick-wall interface in the wick domain.

Liquid evaporates from the wick into the vapor core, while vapor condenses from the vapor core into the wick, both occurring along the *y*-direction. Therefore, the *x*-direction velocity is zero at both side of the vapor-wick interface, given in Eq. (15):

$$u_l = u_v = 0 \tag{15}$$

For the wick domain, the *y*-direction velocity at the wick interface is given by Eq. (16):

$$v_l = \frac{m_i''}{\rho_l} \tag{16}$$

For vapor domain, the *y*-direction velocity boundary at the interface is given by Eq. (17):

$$v_v = \frac{m_i^{"}}{\rho_v} \tag{17}$$

where u_l and u_v are the velocity of liquid and vapor in the x-direction, v_l and v_v are the velocity of liquid and vapor in the y-direction, ρ_l and ρ_v are the density of liquid and vapor, and $m_i^{"}$ is the mass flux at the interface.

The Schrage model, which is based on kinetic theory, is used to describe the mass flux at the interface [11]:

$$m_i^{"} = \left(\frac{2\alpha}{2-\alpha}\right)\left(\frac{1}{2\pi R}\right)\left(\frac{P_v}{T_v^{1/2}} - \frac{P_{v-w}}{T_{v-w}^{\ \ 1/2}}\right) \tag{18}$$

where the accommodation coefficient α is 0.03[9], the interfacial mass transfer under different accommodation coefficients is shown in the Fig.3. It can be seen that, even as the accommodation coefficient takes different values, the variation of interfacial mass tends to be consistent. The R is gas constant, P_v and T_v are the local vapor pressure and temperature near the vapor-wick interface, P_{v-w} and T_{v-w} are pressure and temperature at the vapor-wick interface.

The mass flow rate at the interface is calculated as follow:

$$m_i = m_i^{"} \Delta A \tag{19}$$

where m_i is mass flow rate at the interface, ΔA is the area of the interface cell. $m_i < 0$ represents evaporation, $m_i > 0$ represents condensation.

The pressure and temperature at the vapor-wick interface are calculated by Clausius-Clapeyron:

$$P_{v-w} = P_0 \bullet \exp\left[h_{fg}\frac{1}{R}\left(\frac{1}{T_0} - \frac{1}{T_{v-w}}\right)\right] \tag{20}$$

where h_{fg} is the latent heat of evaporation of the working fluid, P_0 and T_0 are the reference pressure and temperature, respectively.

The temperature boundary satisfies both energy conservation and interfacial temperature continuity. The temperature boundary is as follows:

$$\frac{k_w}{\Delta r_w}\left(T_{v-w} - T_w\right) = \frac{k_v}{\Delta r_v}\left(T_v - T_{v-w}\right) + m_i^{"} h_{fg} \tag{21}$$

where k_v is the thermal conductivity of vapor, T_w and T_v are the temperature of wick and vapor cell near the vapor-wick interface, T_{v-w} is the temperature of the vapor-wick interface in the vapor domain., Δr_w is the distance from wick cell centers to the vapor-wick interface. and Δr_v is the distance from vapor cell centers to the vapor-wick interface.

For the vapor domain, the temperature at the vapor-wick interface is given by Eq. (22):

$$T_{v-w} = \frac{\frac{k_w}{\Delta r_w} T_w + \frac{k_v}{\Delta r_v} T_v + m_i^{"} h_{fg}}{\frac{k_w}{\Delta r_w} + \frac{k_v}{\Delta r_v}} \tag{22}$$

For the wick domain, the temperature at the wick-vapor interface given in Eq. (23):

$$T_{v-w} = T_{w-v} \tag{23}$$

Where T_{w-v} is temperature of the wick-vapor interface in the wick domain.

The initial conditions are as follow:

$$T(x, y) = T_{init}(t = 0) = T_{sat} \tag{24}$$

$$P_{op}(t = 0) = P_{sat} \tag{25}$$

3.4. Operation pressure and fluid density

To satisfy mass conservation, the liquid density in the wick decreases correspondingly. Following each time step, the vapor density, liquid density, and operating pressure are updated, the mass of vapor and liquid is calculated as:

$$M_v = M_v^0 + \Delta t\left(\sum_{wick-vapor} -m_i\right) \tag{26}$$

$$M_l = M_l^0 - \Delta t\left(\sum_{wick-vapor} -m_i\right) \tag{27}$$

where M_v^0 and M_l^0 are the mass of vapor and under initial conditions. According to the ideal gas law, the mass of vapor can be expressed as:

$$M_v = \frac{P_{op}}{R}\sum_{vapor}\frac{\Delta V}{T_v} \tag{28}$$

where P_{op} is the operating pressure, ΔV is the volume of the vapor core cell. By combining Eq. (26) and (28), the operating pressure can be expressed as:

$$p_{op} = \frac{M_v^0 + \Delta t\left(\sum_{wick-vapor} -m_i\right)}{\frac{1}{R}\sum_v \frac{\Delta V}{T_v}} \tag{29}$$

The density of vapor and liquid can be expressed as:

$$\rho_v = \frac{P_{op}}{RT_v} \tag{30}$$

$$\rho_l = \frac{M_l}{\varepsilon V_{wick}} \tag{31}$$

where V_{wick} is the volume of the wick domain.

3.5. Discretization and calculation

The simulations are conducted in Fluent 18.0, the convection, diffusion, and pressure gradient terms are discretized using the second-order upwind, central difference, and least squares scheme, respectively. The governing equations are solved by the SIMPLE algorithm. To enhance computational efficiency, dynamic time stepping is implemented through UDF, with an initial step of 0.01 s that gradually increases to 1 s during simulation. The iteration continues until the residuals of the continuity and momentum equations fall below 10^{-4}, and the energy equation residual drops below 10^{-9}. At the same time, the outer wall temperature stabilizes over time, indicating solution convergence.

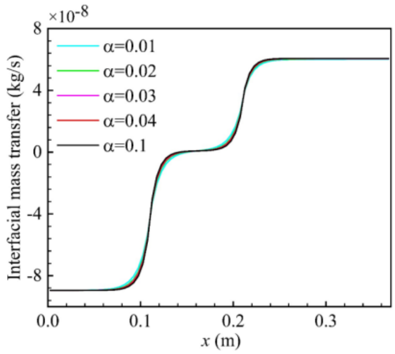

Figure 3. Interfacial mass transfer distribution in the *x*-direction under different accommodation coefficients

4. Calculation of cylindrical heat pipe

4.1. Grid independence check

Fig. 4 shows the grid distribution of the cylindrical heat pipe. The meshes consist of 74×36, 148×36, 296×72 cells, respectively. Fig. 5 shows the operating pressure of the cylindrical heat pipe. The results show that the operating pressure becomes consistent with refinement of meshes. Thus, the 74×36 meshes are selected for subsequent analysis to optimize computational efficiency.

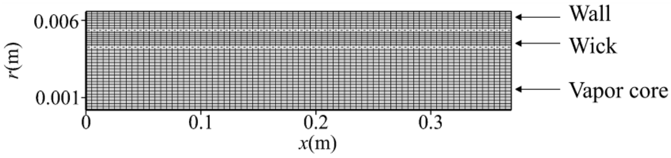

Figure 4. Grid distribution of cylindrical heat pipe

4.2 Validation of numerical methods

The present calculations are validated by available experimental data [12]. Shown in Fig. 6 is the comparison of outside wall temperature. The experimental and numerical simulation results of the outside wall temperature in the evaporation section and the adiabatic section are in good agreement with the present calculations. However, a significant difference is observed in the condensation section, with a maximum temperature difference of 1.2% compared to the experimental data. Due to the thermocouple installed on the condensation section is easily affected by the cooling water, leading to unstable wall temperature measurements.

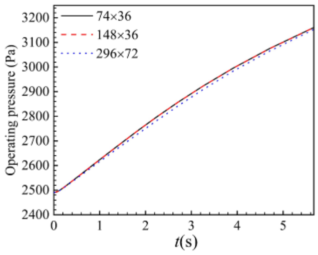

Figure 5. Grid independence of cylindrical heat pipe

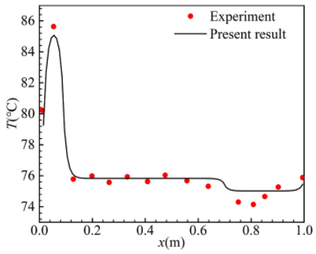

Figure 6. Comparison of outside wall temperature distribution in the *x*-direction model predictions with experiment for cylindrical heat pipe

5. Calculation of flat heat pipe

5.1. Grid independence check

Fig. 7 shows the grid distribution of the flat heat pipe. The meshes with 84×23, 168×28, 252×34 are selected in the *x*-direction and *y*-direction, respectively. The operating pressure of the flat heat pipe is shown in Fig. 8. The results show that mesh refinement leads to consistent variations in the outer wall temperature. Therefore, the mesh with 84×23 cells is selected for the following calculations and analyses.

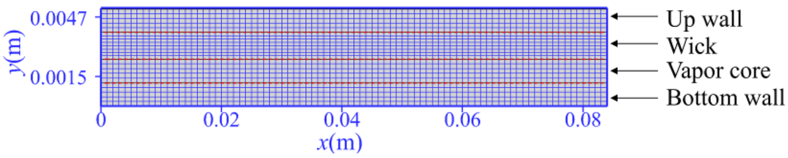

Figure 7. Grid distribution of flat heat pipe

5.2. Validation of numerical methods

Table 1 compares the experimental data [10] for the average outside wall temperature with the present calculations. At heating powers of 10 W and 30 W, the simulation results show less than 0.5% deviation from experimental temperatures across all sections. The present calculations agree well with the literature [10], as shown in Fig.9, which proves the reliability of the present numerical simulation.

Table 1. Comparison of experimental and simulation results with average temperature

Power (W)	Evaporator tem (K)			Adiabatic tem (K)			Condenser tem (K)		
	Experimental	Numerical	Difference%	Experimental	Numerical	Difference%	Experimental	Numerical	Difference%
10	296	295.3	0.24	292.4	292.6	0.068	290.3	290.2	0.034
30	312.1	311.5	0.19	302.1	303.3	0.39	297.3	297.1	0.067

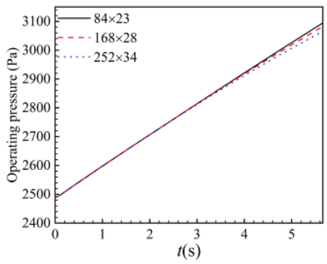

Figure 8. Grid independence of flat heat pipe

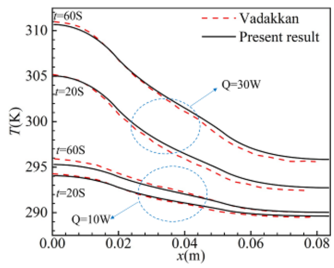

Figure 9. Comparison of outside wall temperature distribution in the *x*-direction model predictions with simulated by vadakkan[10] for flat heat pipe

6. Results and discussions

6.1. Transient characteristics of the flat heat pipe

The transient heat transfer characteristics of the flat heat pipe are analyzed at 30 W heating power. Fig. 10 shows the variation of input and output power. In the start-up stage, the heat pipe exhibits limited heat transfer capability, with most heat being absorbed by the solid wall in the evaporation section. With the continuous heat input, the heat pipe undergoes gradual startup with internal vapor-liquid phase change, enhancing its heat transfer capability. Heat is transported from the evaporator to the condenser, causing the output power to rise and stabilize at a value equaling the input power. Indicating that the heat pipe reaches a stable operating state. The temperature distribution from startup to steady-state is shown in Fig. 11. At the same time, the time required for heat transfer from startup to stabilization reflects the thermal response performance of the heat pipe.

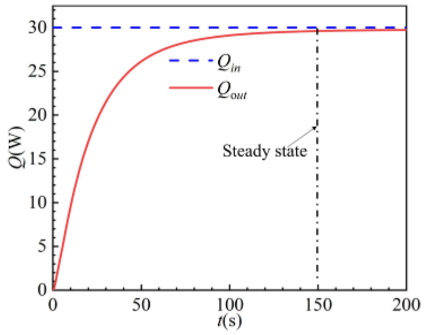

Figure 10. Variation of output power with time

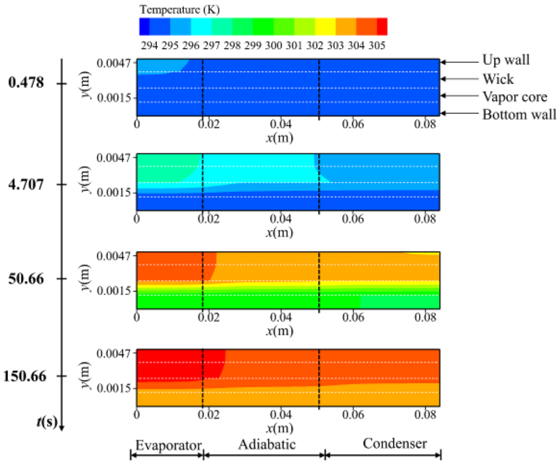

Figure 11. Temperature distribution of heat pipe with time

Heat transfer in a heat pipe involves conduction through the shell and porous medium, working fluid convection, and phase change. During start-up, heat conduction creates a large internal temperature gradient, causing the evaporation rate to exceed the condensation rate. The mass flow rate balance remains consistently negative, as illustrated in Fig. 12. As heating time increases, improved vapor flow heat exchange reduces the temperature difference, driving evaporation and condensation toward equilibrium until the interfacial mass flow rate balance approaches zero. The phenomenon directly causes the operating pressure inside the heat pipe to rise, as shown in Fig. 13. As the heating time increases, the operating pressure also changes from a rapid increase in the start-up phase to slow convergence to a stable value.

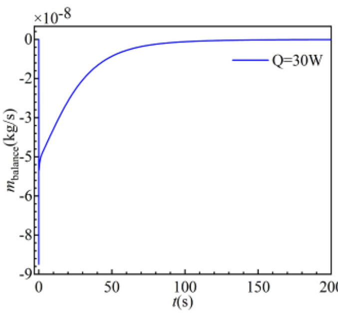

Figure 12. Variation of mass flow rate balance with time

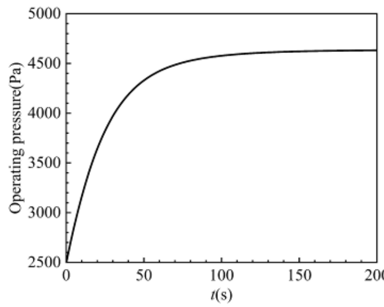

Figure 13. Variation of operating pressure with time

During heat pipe start-up, the working fluid flow undergoes significant variations. Fig. 14 shows the variations of maximum vapor and liquid pressure drop, representing flow losses compensated by the capillary pressure of the wick. Both pressure drops rise sharply in the first 5 s, then stabilize as heating time increases. Similarly, the working fluid velocity follows this trend, as shown in Fig. 15, where the velocity of vapor rises sharply initially and then stabilizes. Due to the rapid rise in the evaporation rate, the velocity of the vapor and liquid increases, which is also influenced by the working medium density. The velocity distribution of vapor is shown in Fig.16. As heating time increases, the evaporation processes intensify, resulting in an increase in vapor mass and density. Fig. 17 shows the dynamic variations in vapor and liquid densities. The vapor velocity rises sharply due to rapid mass transfer rate changes. As the heat pipe stabilizes, the mass transfer rate variation decreases while density gradually increases, causing the vapor velocity to decline slightly and stabilize. In contrast, the liquid velocity remains nearly constant due to minimal density variations.

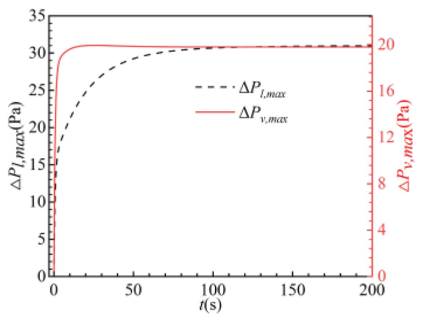

Figure 14. Maximum pressure drop of vapor and liquid with time

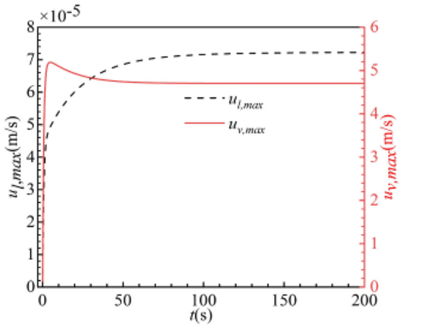

Figure 15. Maximum velocity of vapor and liquid with time

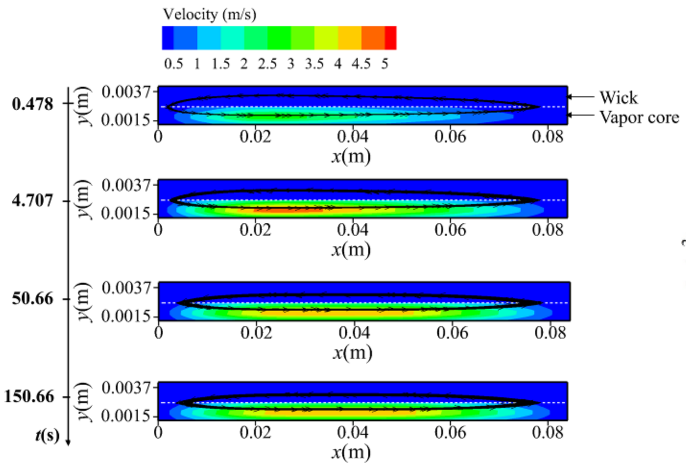

Figure 16. Velocity distribution of vapor in the vapor core with time

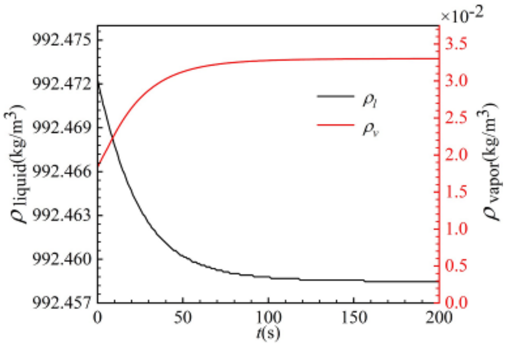

Figure 17. Density of liquid and vapor with time

6.2. Steady-state characteristics of the flat heat pipe

Fig. 18 shows the outside wall temperature distribution as the heating power increases from 10 W to 50 W. It can be seen that the wall temperature increases with heating power, with the average temperature of the evaporation section rising from 298.17 K to 313.25 K and the condensation section from 297.44 K to 310.86 K, showing significant temperature gradients between sections. As heating power increases, more liquid evaporates into vapor. The resulting high-temperature vapor raises both the saturation pressure and temperature in the vapor core. The maximum wall temperature difference, as shown in Fig. 19, increases from 0.75 K to 2.41 K, which also indicates a decline in the overall temperature uniformity of the heat pipe.

Fig. 20 shows the variation of mass flow rate at the vapor-liquid interface. It can be seen that when the heating power is increased from 10 W to 50 W, enhanced heat absorption by the liquid leads to intensified vaporization. Consequently, the interfacial mass flow rate in the evaporation section rises from 1.74×10^{-6} kg/s to 8.95×10^{-6} kg/s. As the fluid flows through the adiabatic section, no phase change occurs at the interface, causing the interfacial mass flow rate to decay to zero. When the vapor reaches the condensation section, the high-temperature vapor releases heat and condenses under cooling, increasing the interfacial mass flow rate from 1.14×10^{-6} kg/s to 5.79×10^{-6} kg/s. The interfacial mass flow rate in the evaporation section consistently surpasses that in the condensation section, demonstrating stronger evaporation than condensation throughout the heat pipe.

The x-direction velocity distribution of vapor at different heating power is shown in Fig. 21. As heating power from 10 W to 50 W, the maximum vapor velocity increases from 2.099 m/s to 5.076 m/s, and the maximum liquid velocity increases from 2.38×10^{-5} m/s to 1.21×10^{-4} m/s. The velocity exhibits the same trend across different heating powers, with values on both sides of the vapor core being lower than those at the middle. Increasing heating power enhances interfacial phase change processes, accelerating vapor flow in the vapor core. The vapor velocity peaks in the adiabatic section, while decreasing in the condensation section. Liquid velocity in the wick shows an inverse trend but follows similar distribution patterns, as shown in Fig. 22.

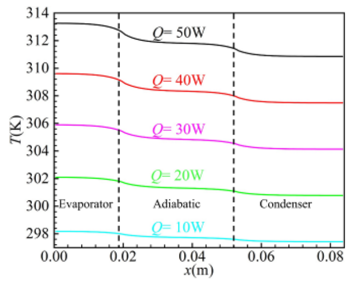

Figure 18. Outside wall temperature distribution in the x-direction at different heating power

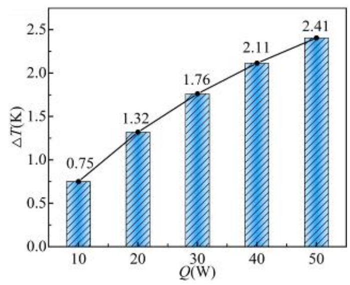

Figure 19. Temperature difference at different heating power

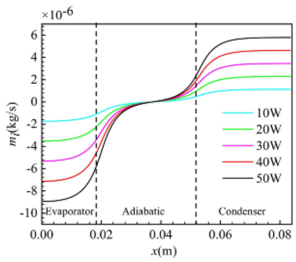

Figure 20. Interfacial mass flow rate distribution in the x-direction at different heating power

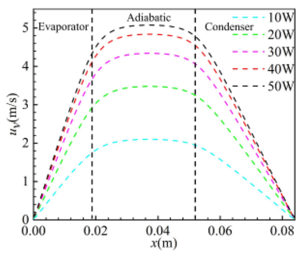

Figure 21. vapor velocity distribution in the x-direction at different heating power

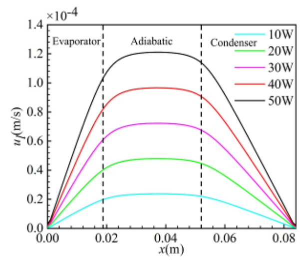

Figure 22. liquid velocity distribution in the x-direction at different heating power

Fig.23 shows variation of vapor pressure drop in the vapor core. Fig.24 shows the variation of liquid pressure drop in the wick. Due to the phase change process, the higher vapor pressure in the evaporation section and the lower in the condensation section, while the liquid pressure exhibits the opposite trend. During vapor flow, inertial and viscous forces induce a pressure drop that decreases along the flow direction. The maximum vapor pressure drop increases with heating power, rising by 13.9 Pa as the power increases from 10 W to 50 W. Similarly, liquid flow in the wick experiences a pressure drop due to frictional and flow resistances, which also decrease along the flow direction. The maximum liquid pressure drop increases with heating power, showing 42 Pa rise when the power increases from 10 W to 50 W. As the heat input increases, the fluid circulation velocity rises, leading to a higher total pressure drop, as shown in Fig. 25. For stable heat pipe operation, the maximum capillary pressure must exceed the combined pressure drop in the wick and vapor core. The relationship of pressure drop is expressed as[13]:

$$\Delta P_{cap} \geq \Delta P_l + \Delta P_v \tag{32}$$

Where ΔP_{cap} is capillary pressure head. However, the capillary pressure head of the wick is limited. The capillary pressure head can be calculated as:

$$\Delta P_{cap} = 2\sigma\left(\frac{\cos\theta_e - \cos\theta_c}{r}\right) \tag{33}$$

Where σ, θ_e, θ_c and r are surface tension, evaporation contact angle, condensation contact angle and curvature radius, respectively.

The maximum capillary pressure head occurs when the evaporation and condensation contact angles are 0° and 90°, and it is calculated as:

$$\Delta P_{cap} = \frac{2\sigma}{r} \tag{34}$$

The curvature radius of screen mesh is given by Eq. (35):

$$r = \frac{1}{2M} \tag{35}$$

As the average temperature of the working medium rises from 293 K to 313 K, its surface tension decreases from 0.0728 N/m to 0.0695 N/m. The maximum capillary pressure of the screen mesh heat pipe ranges from 1833.75 Pa to 1750.63 Pa. The maximum capillary pressure exceeds the total pressure drop.

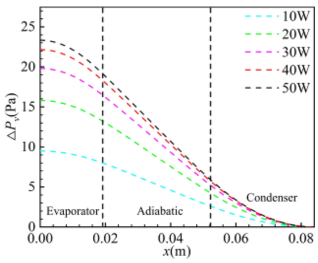

Figure 23. Vapor pressure drop distribution in the *x*-direction at different heating power

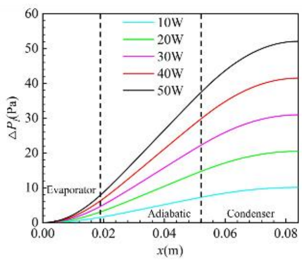

Figure 24. Liquid pressure drop distribution in the *x*-direction at different heating power

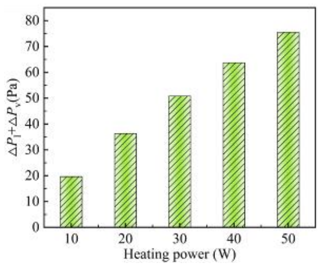

Figure 25. Variation of total pressure drop at different heating power

7. Conclusions

A transient numerical prediction model for triple-phase coupling in both cylindrical and Cartesian coordinates is established in this paper. The transient and steady flow and heat transfer characteristics of flat heat pipe are studied. The main conclusions are as follows:

- In the horizontal configuration of heat pipes, the calculation of flat and cylindrical heat pipes is validated by available experimental data. Good agreements between prediction and measurement are obtained, which proves the capability of the prediction model to simulate phase-change heat transfer and flow in the absence of gravitational effects. Nevertheless, gravity remains an important factor in many practical applications, particularly in non-horizontal orientations. Its effects need to be considered in future work to extend the model's applicability.

- The temperature difference between the evaporation and condensation sections increases with heating power, resulting in reduced temperature uniformity. At the same time, the vapor pressure drop, liquid pressure drop, and total pressure drop all rise with the increased heating power, indicating enhanced internal flow resistance. These results suggest that the heat transfer characteristics and stability of the heat pipe may be compromised under high heating power conditions. Therefore, optimizing the design of heat pipes to improve their performance under high thermal loads is of significant importance.
- The velocities of vapor and liquid show trapezoidal distributions under constant heating power conditions. The velocity gradually increases in the evaporation section, reaches a maximum in the adiabatic section, and decreases in the condensation section. Additionally, as the heating power increases, the velocities of vapor and liquid increase significantly. This finding clearly reveals the flow characteristics of heat pipes under high thermal loads, highlighting that heating power is a critical factor affecting the flow characteristics of the working medium inside the heat pipe.
- In three-dimensional problems, non-uniform heating or cooling source distributions may introduce circumferential temperature gradients, leading to inhomogeneous liquid backflow. Additionally, high-velocity vapor flows may exhibit three-dimensional features such as vortices and flow separation. The simplified two-dimensional symmetric model employed in this study is not applicable to such three-dimensional cases. The effects of three-dimensional dynamics remain an important aspect to be explored in future work.

Nomenclature

C –specific heat capacity $[\mathrm{Jkg^{-1}K^{-1}}]$
k –thermal conductivity $[\mathrm{Wm^{-1}K^{-1}}]$
u –x-direction velocity $[\mathrm{ms^{-1}}]$
v –y-direction velocity $[\mathrm{ms^{-1}}]$
K –permeability $[\mathrm{m^2}]$
C_E –Ergun coefficient
h_{fg} –latent heat of evaporation $[\mathrm{Jkg^{-1}}]$
d –wire diameter $[\mathrm{m}]$
M –mesh number $[\mathrm{m^{-1}}]$
q –heat flux $[\mathrm{Wm^{-2}}]$

Greek symbols

ρ –density $[\mathrm{kgm^{-3}}]$
μ –dynamic viscosity $[\mathrm{Nsm^{-2}}]$
α –accommodation coefficient
σ –surface tension $[\mathrm{Nm^{-1}}]$
ε –porosity
θ –contact angle $[^\circ]$
Δr –distance $[\mathrm{m}]$
ΔT –temperature difference $[\mathrm{K}]$
ΔP –pressure drop $[\mathrm{Pa}]$

References

[1] Tang, H., *et al*., Review of applications and developments of ultra-thin micro heat pipes for electronic cooling, *Applied Energy*, 223 (2018), pp.383–400.
[2] Zhong, G., *et al*., Experimental study of a large-area ultra-thin flat heat pipe for solar collectors

under different cooling conditions, *Renewable Energy*, 149 (2020), pp.1032–1039

[3] Hansel, J. E., *et al*., The liquid-conduction, vapor-flow heat pipe model in Sockeye, *Nuclear Engineering and Design*, 426 (2024), 113359

[4] Fang, W., *et al*., Numerical simulations of the liquid-vapor phase change dynamic processes in a flat micro heat pipe, *International Journal of Heat and Mass Transfer*, 147 (2020), 119022

[5] Annamalai, A. S., *et al*., Experimental investigation and CFD analysis of a air cooled condenser heat pipe, *Thermal Science*, 15 (2011),3, pp.759–772.

[6] Pooyoo, N., *et al*., A Numerical simulation of cylindrical heat pipe considering non-Darcian transport for liquid flow inside wick and mass flow rate at liquid-vapor interface, *International Journal of Heat and Mass Transfer*, 70 (2014), pp.965–978.

[7] Chen, Z., *et al*., Optimization of vapor-liquid channel parameters for ultrathin heat pipe with limited internal cavity, *International Communications of Heat and Mass Transfer*, 142 (2023): 106659.

[8] Li, R., *et al*., Numerical analysis on thermal hydraulic characteristics of mesh-type ultra-thin vapor chambers, *Applied Thermal Engineering*, 236 (2024), 121648

[9] Famouri, M., Numerical Analysis of Phase Change, Heat Transfer and Fluid Flow Within Miniature Heat Pipes, Ph. D. thesis, University of South Carolina, USA, 2017

[10] Vadakkan, U., Transient Three-Dimensional Modeling of Flat Heat Pipes with discrete Heat Sources. Ph. D. Dissertation, thesis, Purdue University, West Lafayette, USA, 2004

[11] Carey, V. P., Liquid-Vapor Phase-Change Phenomena: An Introduction to the Thermophysics of Vaporization and Condensation Processes in Heat Transfer Equipment, CRC Press, Florida, USA, 2020

[12] Faghri, A., *et al*., Experimental and numerical analysis of low-temperature heat pipes with multiple heat sources, *Journal of Heat Transfer*, 113(1991), 3, pp.728-734

[13] Zhuang, J., *et al*., Heat Pipe Technology and Engineering Application, Chemical Industry Press, Beijing, China, 2000

Submitted: 04.7.2025.
Revised: 12.9.2025.
Accepted: 15.9.2025.